



RESEARCH PAPER

Free convection at different locations of adiabatic elliptic blockage in a square enclosure

Sayeda Sadia Billah ^{1,‡}, Muhammad Sajjad Hossain ^{1,*,‡}, Md. Fayz-Al-Asad ^{2,3,‡}, Muhammad Saiful Islam Mallik ^{1,‡}, Sreebash Chandra Paul ^{1,‡}, Md. Jahirul Haque Munshi ^{4,‡} and Md. Manirul Alam Sarker ^{3,‡}

¹Department of Arts and Sciences, Ahsanullah University of Science and Technology (AUST), Dhaka-1208, Bangladesh, ²Department of Mathematics, American International University – Bangladesh, Kuratoli, Khilkhet, Dhaka-1229, Bangladesh, ³Department of Mathematics, Bangladesh University of Engineering and Technology, Dhaka-1000, Bangladesh, ⁴Department of Mathematics, Hamdard University Bangladesh (HUB), Hamdard Nagar, Gazaria, Munshigonj-1510, Bangladesh

*Corresponding Author

‡ sayedasadiabillahs@gmail.com (S.S. Billah); msh80edu@gmail.com (M.S. Hossain); fayzmath.buet@gmail.com (M.F.A. Asad); saiful_math.as@aust.edu (M.S.I. Mallik); sreebash.as@aust.edu (S.C. Paul); jahir.buet.bd@gmail.com (M.J.H. Munshi); masarker45@gmail.com (M.M.A. Sarker)

Abstract

The numerical simulation of free convection flow within a square-shaped enclosure for various orientations of elliptic blockage (EB) is performed in the present study. The bottom wall of the cavity remains uniformly heated, where the left and right (side) walls as well as the boundary wall of the elliptic blockage are insulated and the top wall remains at a cool temperature. As Pr remains constant, the effects of different values of Ra have a great influence on overall fluid flow and temperature gradient for three different locations: bottom elliptic blockage (BEB), center elliptic blockage (CEB) and top elliptic blockage (TEB), as a mass flow circulation has been identified, and a state of equilibrium has been established within the fluid flow simulations along with the isotherm contours. The outcomes of the numerical analysis are presented with the streamlines, isotherms, and variations of the average Nusselt number.

Keywords: Free convection; square cavity; elliptic blockage; streamlines; isotherms; heat transfer rates

AMS 2020 Classification: 76A05; 76D05; 76D07; 76N10

1 Introduction

Over the last decade, free convection in a square cavity has grown in popularity as a research topic. The widespread use of such flows in industrial and natural contexts contributes to their popularity.

The cavity flow with a block inside is considered a benchmark problem in computational fluid dynamics (CFD) and experimental fluid dynamics research. It helps in understanding complex flow behaviors, such as vortex shedding, recirculation zones, and boundary layer development. Also, it helps us understand the flow patterns around obstacles in aerodynamic flow. Aerodynamic performance can be improved and design optimization can be aided by understanding the flow behavior around buildings, aircraft wings, and other structures through the cavity flow with a block inside.

Studies on heat transport can also benefit from this issue. By analyzing the flow and temperature fields within the cavity, researchers can understand heat transfer mechanisms, which are useful in the design of cooling systems, electronic devices, and thermal management solutions. Cavity flows with barriers are useful for research in industries involving fluid mixing, such as chemical engineering and pharmaceuticals. Product quality is enhanced and mixing procedures are optimized by having a better understanding of how fluids interact and mix inside the cavity. Additionally, it can shed light on these kinds of limited flow phenomena. Cavity flow with an internal block is a useful instrument for studying fluid dynamics that may be applied in many different industrial and engineering fields. When designing chemical reactors, food processing machinery, and filtration systems, among other industrial processes, cavity flows with blocks inside can be analyzed to help maximize efficiency. The study of cavity flow may also be beneficial for cardiovascular disorders and the improvement of medical devices such as stents and prosthetic heart valves. It is used in the environmental field to estimate erosion patterns and sediment transformation, among other things. That's why, recent attention has been drawn to the phenomenon of natural convection in fluid flow within a square cavity containing elliptical blockages oriented in various ways. This intriguing phenomenon has also emerged as a pivotal subject in diverse thermal engineering applications, such as reactor insulation, fire prevention, safeguarding electronic equipment, controlling the dispersion of chemical pollutants in water-saturated oil, and optimizing the solidification process in casting. In industrial practice, square cavities, along with other geometric shapes like triangles and cylinders, are commonly employed.

Saury et al. [1] studied free convection in the cavity, where the suppositions allow for the calculation of Rayleigh number values leading to 1.2×10^{11} at ($T = 20^{\circ}\text{C}$). Sajjadi et al. [2] examined turbulent flow in a square cavity, where the streamlines, the isotherm counters, and the local and the average Nusselt number all show the impact of an increase in the Rayleigh number. Shati et al. [3] studied radiation and turbulent fluid flow in square & rectangular cavity, which provides an equation for the mean Nusselt number with no radiation as a function of Prandtl Grashof and numbers. Estebe et al. [4] provided the validation of turbulent fluid flow in a square cavity and a 3D simulation's findings were presented together with an estimation of the cooling system's performance. Choi et al. [5] performed the simulation of turbulent free convection in rectangular cavities and the relative effectiveness of turbulence models is investigated, and both their advantages and disadvantages are discussed. Jani et al. [6] analyzed the impact of MHD in a square cavity and found that the strength of the magnetic field and the Rayleigh number play a great role in the overall simulation. The natural convection of differentially heated enclosures was studied by Butler et al. [7]. The contact between the cylinder and cavity results in an increase in cylinder heat transfer. Xin et al. [8] studied turbulent natural convection in partially heated cavities and showed that the thin stratification is caused by surface radiation. Carvalho et al. [9] studied turbulent free convection in a porous square cavity and discovered that the Nusselt number decreases when the material porosity is raised. Kefayati et al. [10] performed Lattice Boltzmann's exploration of free convection, where the findings showed that at large Rayleigh

numbers, the magnetic field enhances the action of nanoparticles.

Bahoosh et al. [11] numerically examined the fluid flow in a square cavity, where the rotational direction was either inside or outside, and the tilting angles were either 3 or 5 degrees. Jani et al. [12] surveyed free convection in the square cavity and demonstrated that for large Rayleigh numbers, positioning a hot fin in the center of the lower wall has a more notable impact on the flow region and heat transfer within the cavity. Asad et al. [13] examined the effects of twice stratification and various fluid characteristics on the chemically acting upper-convected Maxwell fluid. Islam et al. [14] studied the influence of MHD on the unsteady flow for $Fe_3O_4 - H_2O$ and $TiO_2 - H_2O$ based nanofluids within a square cavity. After comparing, they found a notable difference between their heat transport rates. Asad et al. [15] numerically examined the effect of magneto-combined convection heat transmission of fin length in the lid-driven curvy enclosure. Sajjadi et al. [16] performed a simulation of turbulent free convection utilizing the Lattice Boltzmann method, where heat transfer decreased as the Rayleigh number changed. Miroshnichenko et al. [17] looked into a comparative study of standard $\kappa - \epsilon$ and $\kappa - \omega$ turbulence models and found that the usual model performed better. Tabet et al. [18] investigated convection in a partially heated square cavity, where the outlines of temperature and the evolution of the Nusselt number were provided for several Rayleigh numbers. Zhao et al. [19] scrutinized the field flow of convection and the findings demonstrated the ability of the current method to exactly model the convection difficulties associated with unstable natural processes and are all in strong agreement with individuals found in the literature. Aithal et al. [20] examined turbulent flow in a square cavity and achieved that the Rayleigh number increased and the average and peak Nusselt numbers almost doubled. Massinissa et al. [21] studied the characteristics of different Prandtl numbers, where the increase of Prandtl and Rayleigh numbers had turned the flow field slightly more prominent.

Benchabi et al. [22] analyzed 2D simulation of natural convection in a square cavity and obtained the influence of Rayleigh number caused by a change in size or a difference in temperature on the thermal and dynamic behavior as well as the intensity of the flow caused by the buoyant force. Solomon et al. [23] studied the effect of the aspect ratio of a square cavity on fluid flow and discovered that the Nusselt number and heat transfer coefficient were notably impacted by the enclosure's AR. Yang et al. [24] provided Rans modelling for temperature modification in couple heat transfer and showed that it can accurately predict the distribution of temperature change within the fluid and solid regions. Razera et al. [25] examined the conserving of semi-elliptical blocks constructed into a rectangular enclosure. The results revealed considerable improvements in the heat transmission and fluid flow performances of roughly 76% and 125%, respectively. Selimefendigil et al. [26] investigated heat transmission and fluid flow in the presence of an elliptically-shaped porous item and found that the mean heat transport rate declines with the optimal value of Nu . Khatamifar et al. [27] studied momentary couple free convection heat transport. They found the thermal conductivity ratio effect around the range of 0.1 – 10, but as the partition changes, the effect turns out to be insignificant as the thermal conductivity ratio is very significant. Devi et al. [28] examined the effects of exterior MHD on non-Newtonian fluid in a square cavity. Results exposed that the buoyant force rises as the temperature gradient increases. Wen et al. [29] investigated to better understand how major temperature fluctuations affect the unstable fluid flow and found that the hot wall region exhibits a boundary layer instability with high-frequency undulations in addition to the top corner impact instability. Goswami et al. [30] calculated free convection in a square cavity and found that the mean Nusselt number grows at $Ra = 10^4$. Hattab et al. [31] studied turbulent natural convection in a square cavity and found that the heat transport was increased with the increase of the volume percentage. Turkyilmazoglu

[32] studied nonuniform heating in free convection and found the best heat deletion rate close to the top wall of a cavity. Bilal et al [33] studied the power law fluid in a square cavity and found that heat conduction rises as the Rayleigh number increases, driven by the generation of temperature variations within the fluid domain. Sondur et al. [34] performed a benchmark simulation on fluid flow inside a square cavity and they showed that the most accurate results were found for the steady flow solver *Open FOAM* which took a comparatively short time. Asad et al. [35, 36] explored the natural convection and heat transmit performance on a curvy enclosure. They detected that the mean Nusselt number expands with expanding undulations number. The study conducted by Hossain et al. [37] examined the impact of a cylinder arranged the phenomenon of free convection contained by a square enclosure. The rectangular bar source of heat in a blocked area for free convection flow over a triangular enclosure was examined by Asad et al. [38]. Furthermore, more information is provided in [39–42] on free convection, the finite element (FE) method, and the properties of heat transport with different geometries.

As per the extensive research works conducted by various scientists, it seems that there is a notable absence of exploration regarding the analysis of free convection flow within a square enclosure concerning the various orientations of elliptic blockage. The lack of research in this area concerns important data related to the characteristics of heat transport, which is crucial for understanding its significance in various industries. The flow patterns within the field have been illuminated by the streamlines, while the thermal distribution has been outlined by the isotherms and the average Nusselt number. For the numerical study, the fluid flow within the cavity is characterized by the Prandtl number, $Pr = 0.71$, and Rayleigh number, $Ra = 10^3 - 10^7$.

2 Problem specification

The physical model under consideration along with important geometrical details is displayed in **Figure 1**. The bottom part of the system is subjected to the uniformly heated temperature (T_h), the left and the right walls are thermally insulated (T_i) and the top wall remains at cold temperature (T_c). An elliptic blockage (EB) is placed in different orientations of that cavity whose bottom wall is kept as thermally insulated (T_i). The fluid's Prandtl number ($Pr = 0.7$), Newtonian properties and laminar fluid movement were all thought to be present. It has been assumed that the fluid's properties are constant.

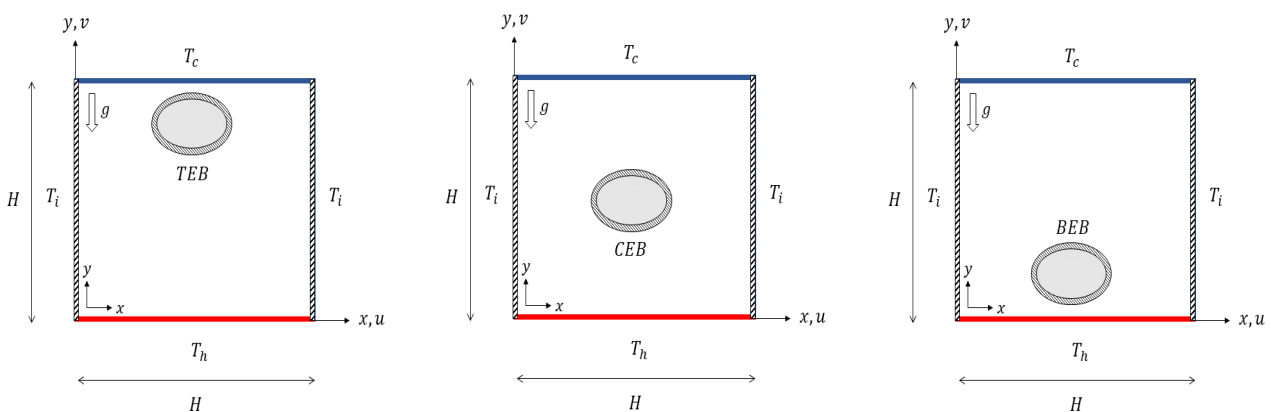


Figure 1. Schematic diagram of physical system

3 Governing equations

The governing equations for the two-dimensional steady flow following the invocation of the equations that govern the steady two-dimensional flow, considering the Boussinesq approximation and neglecting radiation and viscous dissipation, can be formulated in the following manner [6, 33, 39–42]:

Continuity equation:

$$\frac{\partial u}{\partial x} + \frac{\partial v}{\partial y} = 0. \quad (1)$$

Momentum equations:

$$u \frac{\partial u}{\partial x} + v \frac{\partial u}{\partial y} = -\frac{1}{\rho} \frac{\partial p}{\partial x} + \nu \left(\frac{\partial^2 u}{\partial x^2} + \frac{\partial^2 u}{\partial y^2} \right), \quad (2)$$

$$u \frac{\partial v}{\partial x} + v \frac{\partial v}{\partial y} = -\frac{1}{\rho} \frac{\partial p}{\partial y} + \nu \left(\frac{\partial^2 v}{\partial x^2} + \frac{\partial^2 v}{\partial y^2} \right) + \rho g \beta (T - T_c). \quad (3)$$

Energy equation:

$$u \frac{\partial T}{\partial x} + v \frac{\partial T}{\partial y} = \frac{k}{\rho c_p} \left(\frac{\partial^2 T}{\partial x^2} + \frac{\partial^2 T}{\partial y^2} \right). \quad (4)$$

Boundary conditions for governing equations

The followings are the boundary conditions for the current problem:

At the left and right vertical wall:

$$u(0, y) = 0, \quad v(0, y) = 0, \quad \frac{\partial T}{\partial n} = 0.$$

At the bottom wall:

$$u(x, 0) = 0, \quad v(x, 0) = 0, \quad T = T_h.$$

At the top wall:

$$u(x, y) = 0, \quad v(x, y) = 0, \quad T = T_c.$$

At the insider elliptic blockage:

$$u(x, y) = 0, \quad v(x, y) = 0, \quad \frac{\partial T}{\partial n} = 0.$$

Non-dimensional variables

Non-dimensional variables (5) are used for making the governing Eqs. (1)-(4) into dimensionless form are stated as follows:

$$X = \frac{x}{H}, Y = \frac{y}{H}, U = \frac{uH}{\alpha}, P = \frac{pH^2}{\rho\alpha^2}, \theta = \frac{T - T_c}{T_h - T_c}, Pr = \frac{\nu}{\alpha}, Ra = \frac{g\beta(T_h - T_c)H^3}{\alpha\nu}. \quad (5)$$

Non-dimensional governing equations

By using the aforementioned variables, the dimensionless form of the Eqs. (1)-(4) are as follows:

Continuity equation:

$$\frac{\partial U}{\partial X} + \frac{\partial V}{\partial Y} = 0. \quad (6)$$

Momentum equations:

$$U \frac{\partial U}{\partial X} + V \frac{\partial U}{\partial Y} = -\frac{\partial P}{\partial X} + Pr \left(\frac{\partial^2 U}{\partial X^2} + \frac{\partial^2 U}{\partial Y^2} \right), \quad (7)$$

$$U \frac{\partial V}{\partial X} + V \frac{\partial V}{\partial Y} = -\frac{\partial P}{\partial Y} + Pr \left(\frac{\partial^2 V}{\partial X^2} + \frac{\partial^2 V}{\partial Y^2} \right) + RaPr\theta. \quad (8)$$

Energy equation:

$$U \frac{\partial \theta}{\partial X} + V \frac{\partial \theta}{\partial Y} = \left(\frac{\partial^2 \theta}{\partial X^2} + \frac{\partial^2 \theta}{\partial Y^2} \right). \quad (9)$$

The heat transfer coefficient which is the local Nusselt number and mean Nusselt number is defined by

$$Nu_{local} = -\frac{\partial \theta}{\partial n} \text{ and } Nu_{av} = \int_0^1 Nu_{local} dx, \quad (10)$$

respectively, where the normal orientation of a plane is indicated by n .

Boundary conditions for non-dimensional governing equations

The dimensionless boundary conditions which are considered can be expressed as:

At the left and right vertical wall:

$$U = 0, V = 0, \frac{\partial \theta}{\partial n} = 0.$$

At the bottom wall:

$$U = 0, V = 0, \theta = 1 \text{ (Uniformly heated).}$$

At the top wall:

$$U = 0, V = 0, \theta = 0.$$

At the insider elliptic blockage:

$$U = 0, \quad V = 0, \quad \frac{\partial \theta}{\partial n} = 0.$$

4 Method of solution

For solving governing Eqs. (7)-(9), the Galerkin finite element method [43, 44] has been utilized. Eq. (6) is employed as a constraint owing to the conservation of mass. This constraint may be utilized to earn pressure distribution [43, 44]. Regarding the resolution of Eqs. (7)-(9), Eq. (6) is being influenced by the introduction of a penalty parameter, denoted as γ , while the pressure P is being replaced with the subsequent expression [43], which is as follows:

$$P = -\gamma \left(\frac{\partial U}{\partial X} + \frac{\partial V}{\partial Y} \right). \tag{11}$$

Value of $\gamma = 10^7$ perfectly fulfills Eq. (7). Eq. (11) is employed to simplify the expressions in Eqs. (8)-(9), as follows:

$$U \frac{\partial U}{\partial X} + V \frac{\partial U}{\partial Y} = \gamma \frac{\partial}{\partial X} \left(\frac{\partial U}{\partial X} + \frac{\partial V}{\partial Y} \right) + Pr \left(\frac{\partial^2 U}{\partial X^2} + \frac{\partial^2 U}{\partial Y^2} \right), \tag{12}$$

$$U \frac{\partial V}{\partial X} + V \frac{\partial V}{\partial Y} = \gamma \frac{\partial}{\partial Y} \left(\frac{\partial U}{\partial X} + \frac{\partial V}{\partial Y} \right) + Pr \left(\frac{\partial^2 V}{\partial X^2} + \frac{\partial^2 V}{\partial Y^2} \right) + RaPr\theta. \tag{13}$$

Value of U, V and θ are expanded as:

$$U \approx \sum_{k=1}^N U_k \Phi_k(X, Y), \quad V \approx \sum_{k=1}^N V_k \Phi_k(X, Y), \quad \theta \approx \sum_{k=1}^N \theta_k \Phi_k(X, Y). \tag{14}$$

By using the fact that $X \geq 0$ and $Y \leq 0$, the following equations are formed in the domain Ω ,

$$\begin{aligned} R_1^{(1)} = & \sum_{k=1}^N U_k \int_{\Omega} \left[\left(\sum_{k=1}^N U_k \Phi_k \right) \frac{\partial \Phi_k}{\partial X} + \left(\sum_{k=1}^N U_k \Phi_k \right) \frac{\partial \Phi_k}{\partial Y} \right] \Phi_i dXdY \\ & + \gamma \left[\sum_{k=1}^N U_k \int_{\Omega} \frac{\partial \Phi_i}{\partial X} \frac{\partial \Phi_k}{\partial X} dXdY + \sum_{k=1}^N V_k \int_{\Omega} \frac{\partial \Phi_i}{\partial X} \frac{\partial \Phi_k}{\partial X} dXdY \right] \\ & + Pr \sum_{k=1}^N U_k \int_{\Omega} \left[\frac{\partial \Phi_i}{\partial X} \frac{\partial \Phi_k}{\partial X} + \frac{\partial \Phi_i}{\partial Y} \frac{\partial \Phi_k}{\partial Y} \right] dXdY, \end{aligned} \tag{15}$$

$$\begin{aligned}
 R_1^{(2)} = & \sum_{k=1}^N V_k \int_{\Omega} \left[\left(\sum_{k=1}^N U_k \Phi_k \right) \frac{\partial \Phi_k}{\partial X} + \left(\sum_{k=1}^N V_k \Phi_k \right) \frac{\partial \Phi_k}{\partial Y} \right] \Phi_i dXdY \\
 & + \gamma \left[\sum_{k=1}^N U_k \int_{\Omega} \frac{\partial \Phi_i}{\partial X} \frac{\partial \Phi_k}{\partial X} dXdY + \sum_{k=1}^N V_k \int_{\Omega} \frac{\partial \Phi_i}{\partial X} \frac{\partial \Phi_k}{\partial X} dXdY \right] \\
 & + Pr \sum_{k=1}^N V_k \int_{\Omega} \left[\frac{\partial \Phi_i}{\partial X} \frac{\partial \Phi_k}{\partial X} + \frac{\partial \Phi_i}{\partial Y} \frac{\partial \Phi_k}{\partial Y} \right] dXdY \\
 & + RaPr \int_{\omega} \left(\sum_{k=1}^N \theta_k \Phi_k \right) \Phi_i dXdY,
 \end{aligned} \tag{16}$$

and

$$\begin{aligned}
 R_1^{(3)} = & \sum_{k=1}^N U_k \int_{\Omega} \left[\left(\sum_{k=1}^N U_k \Phi_k \right) \frac{\partial \Phi_k}{\partial X} + \left(\sum_{k=1}^N V_k \Phi_k \right) \frac{\partial \Phi_k}{\partial Y} \right] \Phi_i dXdY \\
 & + \sum_{k=1}^N \theta_k \int_{\Omega} \left[\frac{\partial \Phi_i}{\partial X} \frac{\partial \Phi_k}{\partial X} + \frac{\partial \Phi_i}{\partial Y} \frac{\partial \Phi_k}{\partial Y} \right] dXdY.
 \end{aligned} \tag{17}$$

The expressions given by Eqs. (15)-(17) can be depicted using matrix notation as follows:

$$(K_1 + \gamma K_2)a = F, \tag{18}$$

where K_1, K_2 matrices are derived from the Jacobian of the residuals, ' a ' signifies the unidentified vector, as $\gamma \sim 10^7$, Eq. (6) is better content, which tends to the following:

$$K_1 a = \frac{F}{\gamma}. \tag{19}$$

The Newton-Raphson method has been employed to address the non-linear Eqs. (15)-(17), yielding the subsequent linear system as follows:

$$J(a^n)[a^n - a^{n+1}] = R(a^n). \tag{20}$$

At the end of the iterative process, $\left[\sum (R_i^j)^2 \right]^{0.5} \leq 10^{-6}$ is utilized. Each of the nine-node bi-quadratic elements that we applied is approximated from $(X - Y) \rightarrow (\zeta - \eta)$, which are:

$$X = \sum_{i=1}^9 X_i \Phi_i(\zeta - \eta) \text{ and } Y = \sum_{i=1}^9 Y_i \Phi_i(\zeta - \eta), \tag{21}$$

on the $(\zeta - \eta)$ domain, where $\Phi_i(\zeta, \eta)$ are the local bi-quadratic basis functions. The following

assumptions can be used to analyze the domain of the integrals in Eqs. (15)-(17):

$$\begin{bmatrix} \frac{\partial \Phi_i}{\partial X} \\ \frac{\partial \Phi_i}{\partial Y} \end{bmatrix} = \frac{1}{|J|} \begin{bmatrix} \frac{\partial Y}{\partial \eta} & -\frac{\partial Y}{\partial \zeta} \\ -\frac{\partial X}{\partial \eta} & \frac{\partial X}{\partial \zeta} \end{bmatrix} \begin{bmatrix} \frac{\partial \Phi_i}{\partial \zeta} \\ \frac{\partial \Phi_i}{\partial \eta} \end{bmatrix} \text{ and } dXdY = |J|d\zeta d\eta, \quad (22)$$

where $J = \left| \frac{\partial(X,Y)}{\partial(\zeta,\eta)} \right|$. According to Eq. (10), the local Nusselt number takes a normal derivative that can be found over a bi-quadratic basis set in the $(\zeta - \eta)$ domain by using Eqs. (21) and (22).

Evaluation of stream function

The 2D stream function is formed from the velocity elements U and V , as follows:

$$U = \frac{\partial \psi}{\partial Y}, V = -\frac{\partial \psi}{\partial X}, \quad (23)$$

which can be utilized in the single equation as,

$$\frac{\partial^2 \psi}{\partial X^2} + \frac{\partial^2 \psi}{\partial Y^2} = \frac{\partial U}{\partial Y} - \frac{\partial V}{\partial X}. \quad (24)$$

The Galerkin finite element method is utilized to derive the subsequent linear resultant equations for Eq. (14). This is achieved by replacing the stream function with $\{\Phi_k\}_{k=1}^N$ as $\psi = \sum_{k=1}^N \psi_k \Phi_k(X, Y)$ from Eq. (24):

$$\begin{aligned} R_i^{(s)} &= \sum_{k=1}^N \psi_k \int_{\Omega} \left[\frac{\partial \Phi_i}{\partial X} \frac{\partial \Phi_k}{\partial X} + \frac{\partial \Phi_i}{\partial Y} \frac{\partial \Phi_k}{\partial Y} \right] dXdY \\ &+ \sum_{k=1}^N U_k \int_{\Omega} \Phi_i \frac{\partial \Phi_k}{\partial Y} dXdY - \sum_{k=1}^N V_k \int_{\Omega} \Phi_i \frac{\partial \Phi_k}{\partial X} dXdY. \end{aligned} \quad (25)$$

Through the utilization of $\psi = 0$, the no-slip boundary condition is imposed due to the absence of cantankerous flows.

5 Model algorithm

The initial goal of the iterative Newton-Raphson algorithm is to analyze the discrete dimensions of continuity, momentum, and energy equations in order to assess the significance of speed and temperature. It is necessary to take into account the initial values of the variables. After that matrix factorization was found clearly discussed by Rahman et al. [45] before convergence criteria. When the convergence criteria are satisfied, the numerical solutions for the variables are then obtained. A straightforward algorithm is depicted in the flow chart (see Figure 2) below.

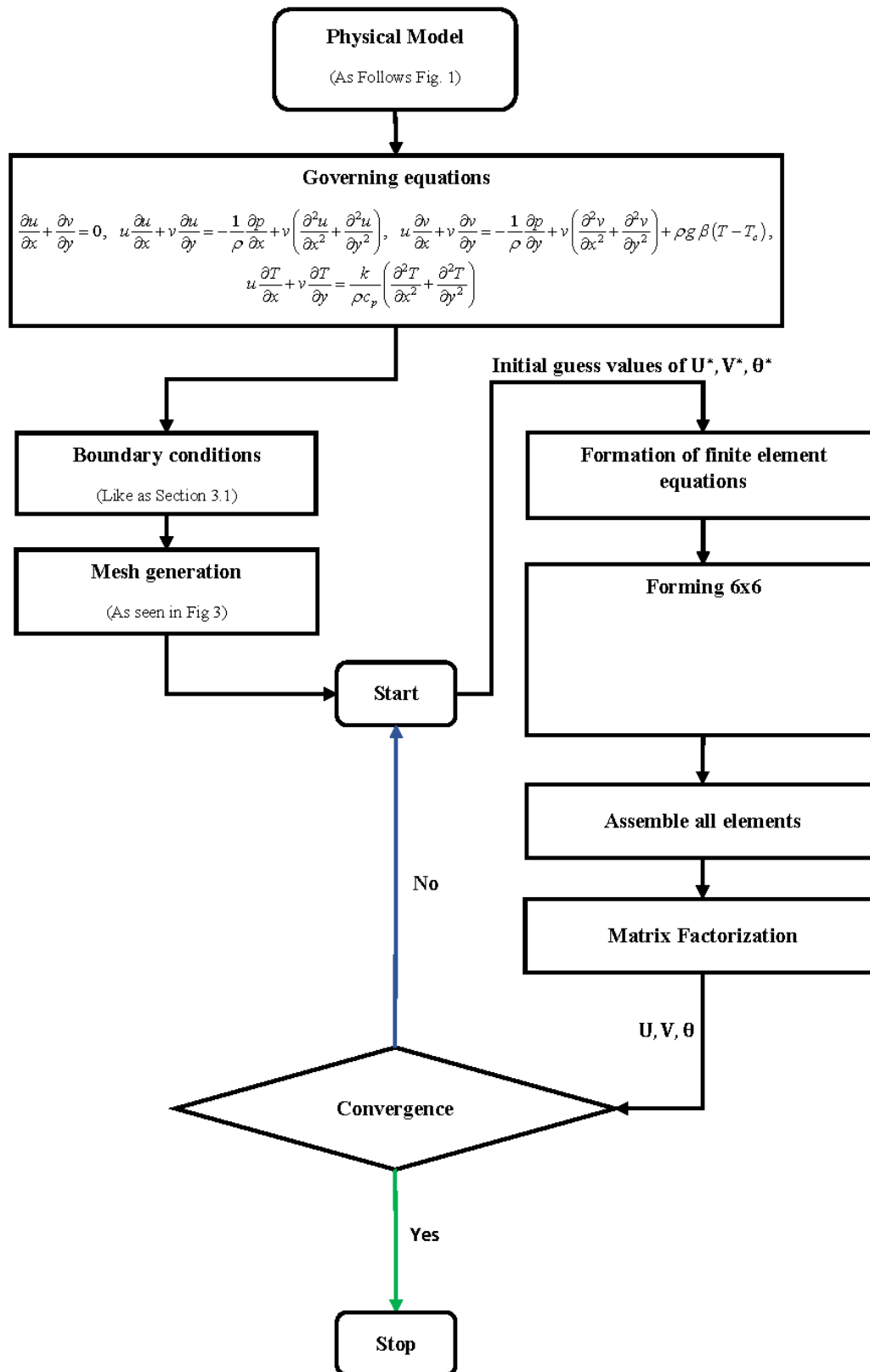


Figure 2. Flow algorithm diagram of the computational process

6 Test for grid sensitivity

Significant progress has been made in the exploration of grid-independent solutions for the field variables, yielding promising initial outcomes. A comprehensive analysis has been carried out to assess the precision of grid performance and ascertain the most suitable grid quantity. To attain grid-independent results for a square cavity with EB, a thorough investigation involving grid refinement was conducted for $Pr = 0.71$ and $Ra = 10^5$. In Figure 3, the convergence of the Nusselt number (Nu) at the heated surface is depicted as grid refinement is implemented. Grid independence has been achieved with the utilization of 31256 nodes. However, as the number of mesh elements increases beyond this point, the impact on Nu becomes negligible, rendering the changes insignificant. Therefore, any insignificance observed prior to the 31256 nodes should not be regarded as an indication of grid independence. For the grid independence tests, six distinct non-uniform grids were employed, each of them characterized by varying numbers of nodes and elements. The configurations used are as follows: 16012 nodes, 3698 elements; 18564 nodes, 3785 elements; 21343 nodes, 4134 elements; 23412 nodes, 4421 elements; 31256 nodes, 5893 elements; and 37895 nodes, 6598 elements. These details are presented in Table 1.

Table 1. Grid independence test at $Pr = 0.71$ and $Ra = 10^5$

Nodes	16012	18564	21343	23412	31256	37895
Elements	3698	3785	4134	4421	5893	6598
Nu_{av}	0.140123	0.140933	0.141894	0.144403	0.145403	0.145403
Time(s)	15.321	19.204	22.532	26.577	36.625	38.442

Based on the provided values, it is recommended to consistently utilize 31256 nodes and 5893 elements throughout the simulation to effectively locate the required accuracy and computing time. Figure 4-Figure 5 display the mesh design and finite element discretization of a domain respectively for this research work.

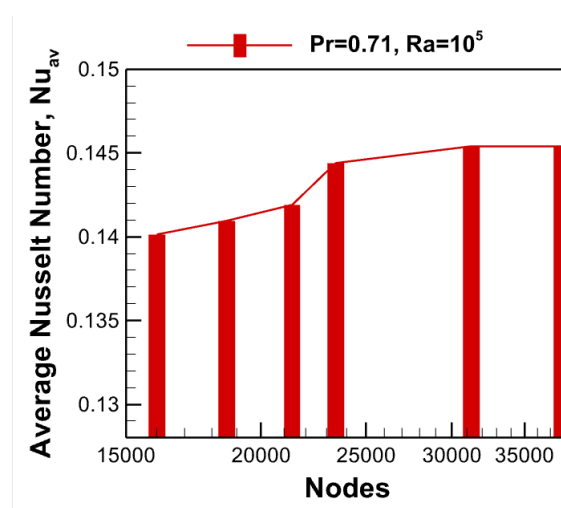


Figure 3. Convergence of Nusselt number with grid refinement for $Pr = 0.71$, and $Ra = 10^5$

7 Numerical validation

For the validation of the accuracy of the numerical technique, the problem that is considered for the present work was solved with $Pr = 0.71$, $Ha = 50$ and $Ra = 10^4$ for stream function

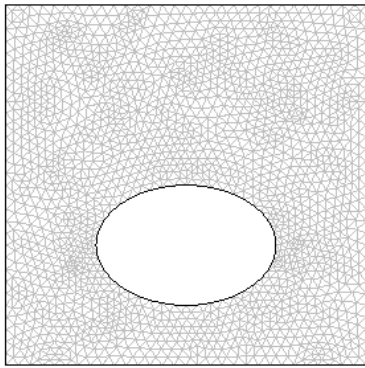


Figure 4. The mesh design

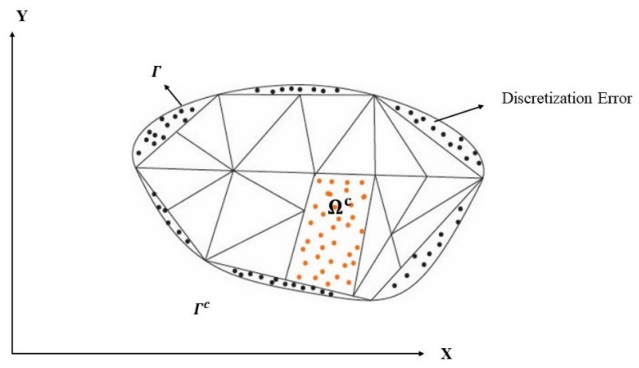
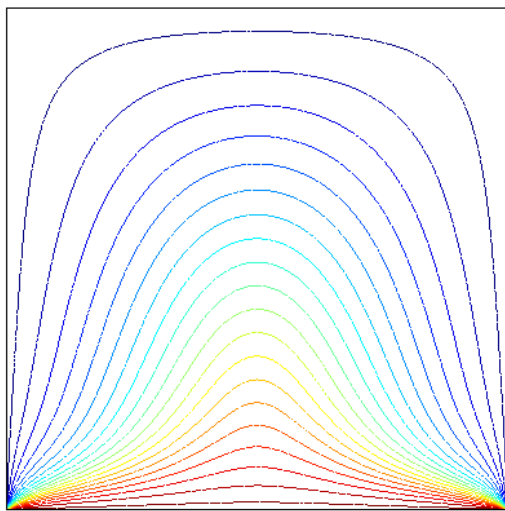


Figure 5. Finite elements discretization of a domain

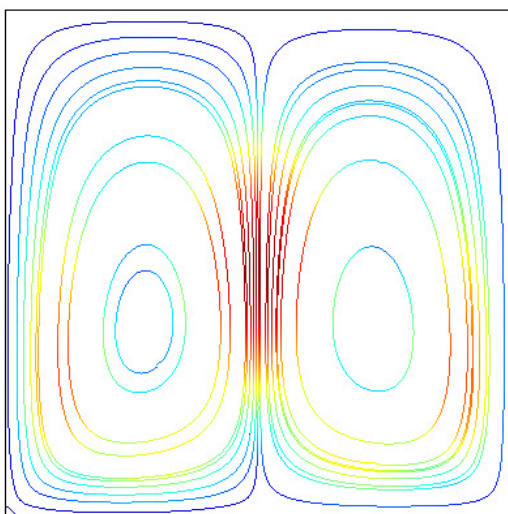
(streamlines) and isotherms within a square cavity. The result was checked by comparing it with the paper of Jani et al. [6], and found a good agreement which is shown in Figure 6.



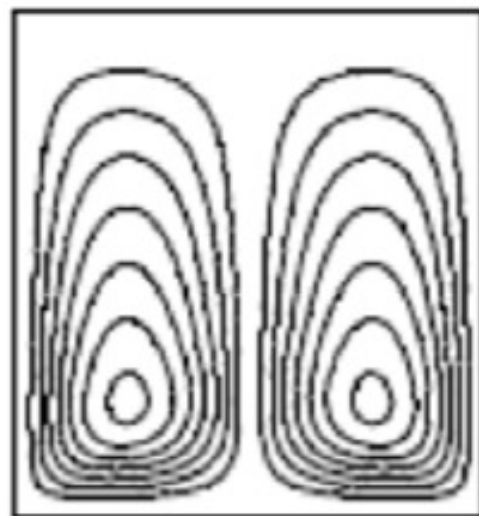
(a) Isotherms for present research work



(b) Isotherms for Jani et al. [6]



(c) Streamlines for present research work



(d) Streamlines for Jani et al. [6]

Figure 6. Stream function and isotherms of present work compared with Jani et al. [6] for $Pr = 0.71$, $Ha = 50$ and $Ra = 10^4$

8 Results and discussion

A numerical study on free convection flow within a square enclosure for various orientations of elliptic blockage (EB) has been carried out. The electrically conductive fluid with $Pr = .71$ is being examined within a square cavity in the presence of EB, where other parameters are taken as $Ra = 10^3 - 10^7$. The numerical outcomes have been depicted through visual representations of streamlines and isotherms within the square cavity along with EB, as well as through data on heat transfer rates via average Nusselt numbers.

Streamlines and isotherms: effect of Ra for different locations of EB

Streamlines and isotherms for governing parameters Pr and Ra , along with EB have been shown in [Figure 7-Figure 9](#). The bottom wall of the cavity was uniformly heated and the bottom wall of the EB was thermally insulated. Several eddy circulation cells were circulated from the heating bottom wall due to the heated fluid flow, spinning along the insulated side walls for all governing parameters Pr and Ra . In order to discover the changes in streamlines and isotherms, a numerical simulation was completed at the bottom wall of the cavity with the elliptic blockage (BEB), at the center of the cavity with the elliptic blockage (CEB), and at the top wall of the cavity with the elliptic blockage (TEB) with $Pr = 0.71$ and $Ra = 10^3 - 10^7$. At the BEB phase, the EB is placed near the bottom wall of the cavity for $Ra = 10^3 - 10^7$ (see [Figure 7a](#)). It is seen from the streamlines that two large eddy circulation cells have been formed at the top of the EB and two vortices have been found at the bottom wall where the left one is significantly smaller than the right one and the right one has a few small vortices inside it. As Ra is considered $Ra = 10^4$, any notable changes have not been found in the streamlines (see [Figure 7b](#)). But when $Ra = 10^5$ is applied, the top two cells become much denser than before and the right bottom big vortex decreases in size as well as the number of embedded vortices decreases to one same vortex (see [Figure 7c](#)). At $Ra = 10^6$, in [Figure 7d](#), the top two cells become much thicker than before where the left cell becomes denser than the right one and also the bottom two vortices are now almost in the same shape and several small vortices have been formed inside them but the right vortex seems thicker than the left one. At 10^7 ([Figure 7e](#)), the top two rotating cells seem to be decreasing in thickness and the left bottom vortex is now in small size without any embedded vortices and the right bottom vortex also decreases in thickness with one small vortex embedded inside it.

From the isotherms, for $Ra = 10^3$ ([Figure 7a](#)), linear lines are found at the top cold wall which begins to turn into non-linear lines near the EB. Dense temperature lines are found at the left and right walls near the EB. The lowest temperature of the cavity $\theta = 0.03$ has been found at the top cold wall and the highest temperature of the cavity $\theta = 0.98$ has been found at the bottom heated wall. The lowest temperature on EB $\theta = 0.28$ has been found at the top cold wall and the highest temperature on EB $\theta = 0.93$ has been found at the bottom heated wall. No significant changes are found for $Ra = 10^4$ ([Figure 7b](#)) in the isotherms. But at $Ra = 10^5$ ([Figure 7c](#)), the shape of the isotherms is notably changed where non-linear lines at the top cold wall grow in numbers and the curved lines at the insulated sidewalls are seen to be changed than before where the temperature lines are becoming denser at the sidewalls. The only changes in temperature are seen for the lowest temperature at the top wall of EB at $\theta = 0.23$. At $Ra = 10^6$ ([Figure 7d](#)), the isotherms are turned to a chaotic shape, where many non-linear lines are formed around the EB. The highest and the lowest temperatures are found to remain unchanged but the lowest temperature at EB changes to $\theta = 0.13$. When $Ra = 10^7$ ([Figure 7e](#)), the highest chaotic stage of the isotherms is discovered where many non-linear curved lines are forming around the EB and the lowest temperature at the EB changes to $\theta = 0.18$. The temperature lines are at the highest dense position at the

insulated side walls. The EB is placed at the center of the cavity, at the CEB phase, for $Pr = 0.71$ and $Ra = 10^3 - 10^7$ (see Figure 8a). It is viewed that four symmetric eddy circulation cells are formed around the EB in the streamlines, where the top two cells are much more dense than the bottom two cells. As Ra changes to $Ra = 10^4 - 10^5$ (Figure 8b – Figure 8c), no significant changes have been found in the fluid flow. Slight changes are found when $Ra = 10^6$ (see Figure 8d) is applied. The top two cells become much more packed than before, where the right cell is thicker than the left one. At $Ra = 10^7$, the highest thickness of the eddy circulation cells has been seen in the fluid flow, where the top left cell is the thickest of all. Also, the space between the top cells and the bottom cells grew larger than in the previous simulations. As for the isotherms, at $Ra = 10^3$ (Figure 8a), linear smooth curves are only seen at the top and the bottom wall and the rest are non-linear lines where most of them are generated from the surface of the EB. The temperature curves are thickest at the insulated left and right side walls. The lowest temperature of the cavity is $\theta = 0.03$ and the highest temperature of the cavity is $\theta = 0.98$ which has been found for convectational fluid flow. In Figure 8b, the lowest temperature of the surface of EB is $\theta = 0.23$ and the highest temperature of the surface of EB is $\theta = 0.78$. At $Ra = 10^4$ (Figure 8b), no notable changes are found at the temperature curve. But at $Ra = 10^5$ (Figure 8c), curves are taking chaotic forms, which seem to be drawing to the surface of EB. The changes in temperature are seen only on the surface of the EB, the lowest temperature $\theta = 0.13$ and the highest temperature $\theta = 0.83$. When $Ra = 10^6$ (Figure 8d), it is now in a complete chaotic form, where the highest dense curves are seen at the two side walls, the curves at the top and the bottom wall are also found in dense position. At the surface of EB, the lowest and the highest temperature are respectively $\theta = 0.18$ and $\theta = 0.88$. At $Ra = 10^7$ (Figure 8e), isotherms are taking a complete new shape, where the curves at the two side walls along with the top and bottom walls are at the peak of density. The only change is found at the lowest temperature of the surface of the EB, $\theta = 0.13$. At the TEB phase, where the EB is placed at the top of the cavity, for $Pr = 0.71$ and $Ra = 10^3$ (Figure 9a), two large rotating eddies are found at the bottom of the EB in the streamlines, where the right one is much thicker than the left one. Two distinct vortices have also been formed at the EB while the right one is much bigger than the left one. When Ra increases to $Ra = 10^4$ (Figure 9b), the density of the two large eddies is increased than before and it is continually increasing at $Ra = 10^5 - 10^6$ (Figure 9c – Figure 9d). A thick borderline has formed around the two vortices at the top wall, the right vortex is now smaller than the left one. At $Ra = 10^7$ (Figure 9e), the density of the left eddy circulation cell is decreased than the left one, and the shape of the two vortices at the top wall is slightly changed. In the case of the isotherms study, at $Ra = 10^3$ (Figure 9a), only a linear temperature curve is seen at the bottom wall and the rest of them are non-linear curves, attracting to the surface of the EB. The density of the temperature curves is the highest at the insulated left and right sidewalls. The lowest temperature of the cavity is found at $\theta = 0.03$ and the highest temperature of the cavity is found at $\theta = 0.98$. Also, the lowest temperature of the surface of the EB is recorded at $\theta = 0.08$ and the highest temperature of the surface of the EB is recorded at 0.68 . No significant changes are found in the isotherms for $Ra = 10^4$ (Figure 9b). But at $Ra = 10^5$ (Figure 9c), the temperature curves turn to chaotic shapes, and the highest curvature is found at the bottom of the EB. Only changes in the temperature value are found on the surface of the EB where the temperature is highest at $\theta = 0.78$. At $Ra = 10^6$ (see Figure 9d), isotherms are changed completely and the density of the curves at the sidewalls is increased a lot. As before, only changes of temperature value are found for the surface of the EB, lowest at $\theta = 0.03$ and highest at $\theta = 0.88$. And when Ra increases to $Ra = 10^7$ (Figure 9e), temperature curves are at the peak of the chaotic stage, where the density of curves at the side walls is higher than before. Similarly, only changes are found for the surface of the EB for the lowest temperature at $\theta = 0.08$ and the highest temperature at $\theta = 0.83$ due to the effect of convection fluid flow.

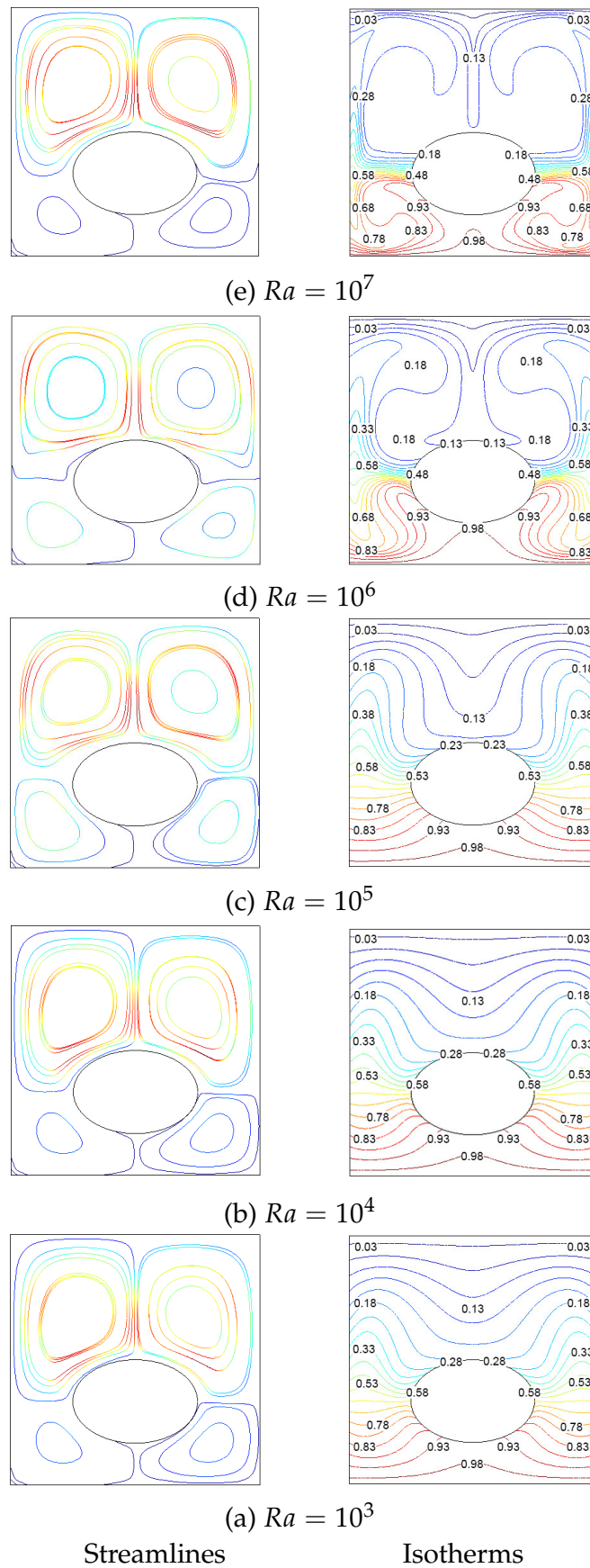


Figure 7. Streamlines and Isotherms for $Pr = 0.71$ and $Ra = 10^3 - 10^7$ for BEB

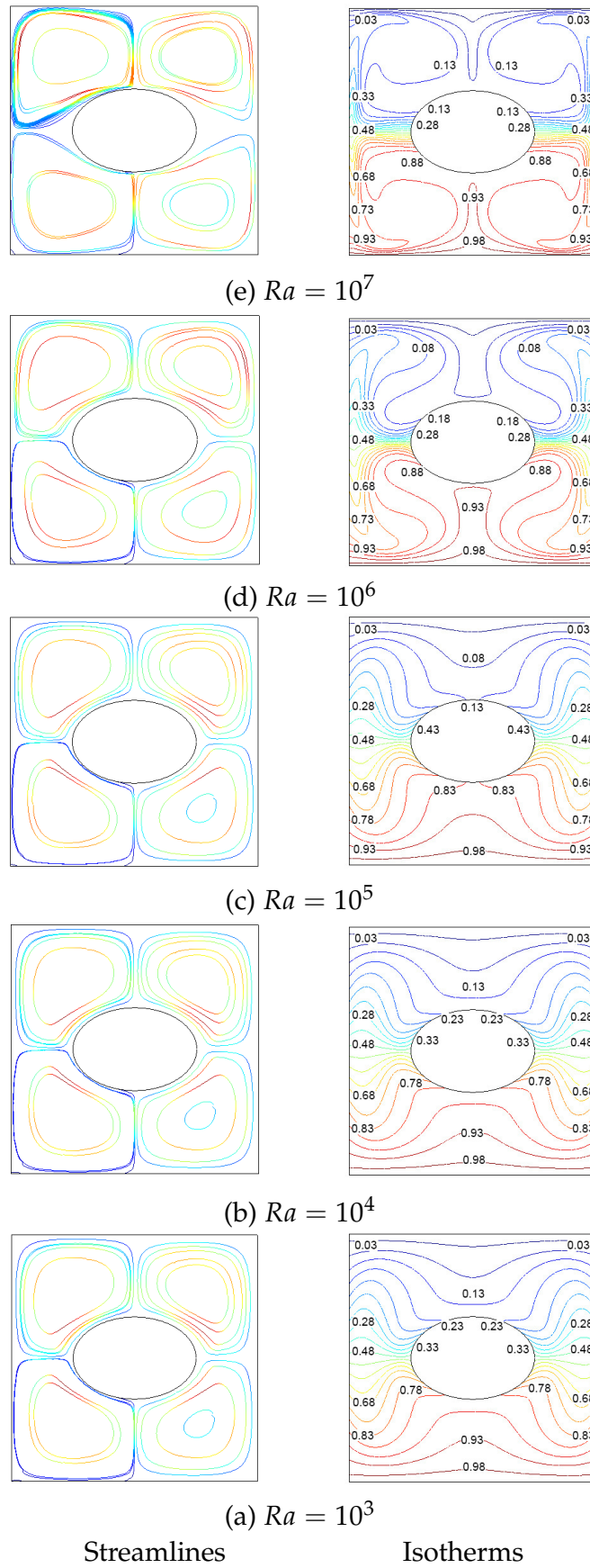


Figure 8. Streamlines and Isotherms for $Pr = 0.71$ and $Ra = 10^3 - 10^7$ for CEB

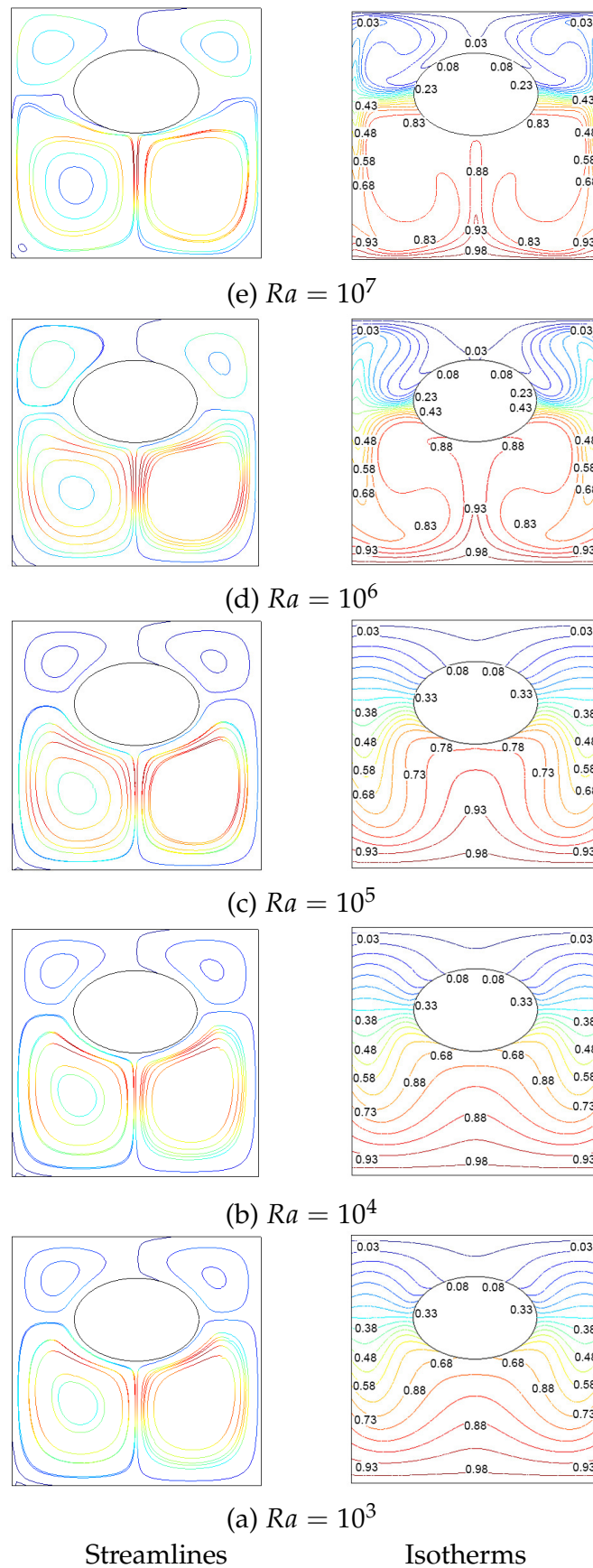


Figure 9. Streamlines and Isotherms for $Pr = 0.71$ and $Ra = 10^3 - 10^7$ for TEB

Heat transfer rates: Nu_{av} vs Ra for bottom wall of the cavity and insulated EB

The overall changes of average Nusselt number with increasing Rayleigh number for $Pr = 0.71$ and $Ra = 10^3 - 10^7$, are displayed in Figure 10-Figure 11 for the heated bottom wall of the cavity and bottom wall of insulated EB for different orientation BEB, CEB, and TEB.

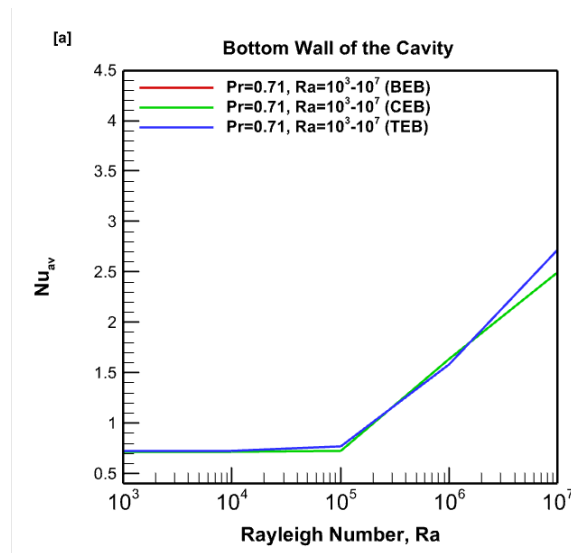


Figure 10. Average Nusselt number for (a) bottom wall of the cavity

From Figure 10, for (a), the heated bottom of the cavity, there is a logarithmic relationship being seen between Nu_{av} and Ra . A slow increase of Nu_{av} is found up to $Ra = 10^5$ for all three different orientations and when $Ra \geq 10^6$, the graph begins to rise for BEB, CEB, and TEB. This happens due to the transition from the conduction phase to the convection phase. The lowest value of Nu_{av} is recorded for $Ra = 10^3$ at CEB and the highest value of Nu_{av} is recorded for $Ra = 10^7$ at TEB. As for (b), the bottom wall of insulated EB, from Figure 11, the gradual increase of Nu_{av} occurs as Ra increases.

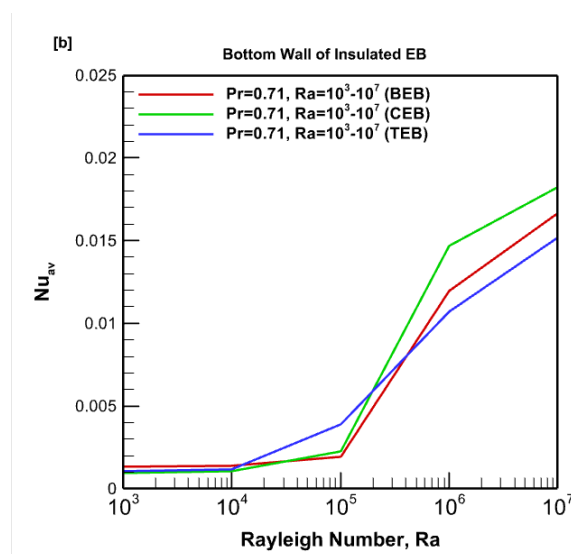


Figure 11. Average Nusselt number for (b) bottom wall of EB

For BEB and CEB orientations, the drastic change in the graph is started from $Ra \geq 10^5$ due to

convective flow, whereas for TEB orientation, it is at $Ra \geq 10^4$. After reaching $Ra = 10^6$, the graph turns to a constant curve up to $Ra \geq 10^7$ for all three locations. The lowest heat transfer rate is found at $Ra = 10^3$ for CEB and the highest value at $Ra = 10^7$ for CEB.

9 Conclusion

An inclusive research work of free convection flow within a square enclosure for various locations of elliptic blockage for $Pr = 0.71$ and $Ra = 10^3 - 10^7$ has been analyzed numerically in the present study. The Galerkin weighted residual technique has been utilized to address the governing parameters Pr and Ra within finite element formulations aimed at solving the governing equations. The results are shown using stream functions, isotherms, heat transfer rates, and average Nusselt numbers, both for the bottom wall of the cavity and the bottom wall of the insulated EB. The key assumptions are concisely outlined as follows:

- Heat transfer mechanisms, flow characteristics, and the distribution of isotherms within the cavity depend exclusively on four key factors: EB, the temperature of the heated bottom wall, and two dimensionless numbers – the Prandtl number (Pr) and the Rayleigh number (Ra).
- The streamlines show that the area around the EB contains multiple vortex cells and swirling eddy currents for all three different orientations.
- At the heated bottom wall of the cavity, Nu_{av} is seen to have a logarithmic relation with Ra at $Pr = 0.71$ and $Ra = 10^3 - 10^7$, due to the transition from the conduction stage to the convection stage. The lowest value of Nu_{av} is recorded for $Ra = 10^3$ at CEB and the highest value of Nu_{av} is recorded for $Ra = 10^7$ at TEB.
- At the bottom wall of insulated EB, Nu_{av} is seen to be increasing with the value of Ra , and a quick change of the graph is found for the flow of strong convection at $Ra = 10^5$ for BEB and CEB and at $Ra = 10^4$ for TEB. At $Ra = 10^6$, a constant increasing graph is found for all three locations which implies invariant heat transfer. The lowest heat transfer rate is found at $Ra = 10^3$ for CEB and the highest value at $Ra = 10^7$ for CEB.

Declarations

List of symbols

C_p	Specific heat at constant pressure (J/kg K)
g	Gravitational acceleration (m/s^2)
h	Convective heat transfer coefficient ($W/m^2 K$)
k	Thermal conductivity of fluid ($W/m K$)
K	Thermal conductivity ratio fluid
N	Non-dimensional distance
Nu_{av}	Average Nusselt number
P	Non-dimensional pressure
p	Pressure
Pr	Prandtl number
Ra	Rayleigh number
T	Non-dimensional temperature
T_c	Cold temperature
T_h	Hot temperature
T_i	Thermal insulated Temperature
U	Dimensionless horizontal velocity
u	Velocity in x-direction (m/s)
V	Dimensionless vertical velocity
v	Velocity in y-direction (m/s)
x, y	Cartesian coordinates
X, Y	Dimensionless cartesian coordinates

Greek symbols

β	Coefficient of thermal expansion (1/K)
ρ	Density of the fluid (kg/m ³)
α	Thermal diffusivity (m ² /s)
$\Delta\theta$	Temperature difference
θ	Fluid temperature
μ	Dynamic viscosity of the fluid (Pa s)
ν	Kinematic viscosity of the fluid (m ² /s)
σ	Fluid electrical conductivity($\Omega^{-1} \text{ m}^{-1}$)

List of abbreviations

BEB	Bottom elliptic blockage
CEB	Center elliptic blockage
EB	Elliptic blockage
TEB	Top elliptic blockage

Use of AI tools

The authors declare that they have not used Artificial Intelligence (AI) tools in the creation of this article.

Data availability statement

All authors declare that data availability is not applicable to this article.

Ethical approval

Not applicable

Consent for publication

Not applicable

Conflicts of interest

The authors declare that they have no known competing financial interests or personal relationships that could have appeared to influence the work reported in this paper.

Funding

Not applicable

Author's contributions

S.S.B.: Writing - first draft, Methodology, Software, Investigation. M.S.H.: Conceptualization, Validation, Methodology, Software, Investigation, Writing - Original Draft, Writing - Review & Editing, Administration, Supervision. M.F.A.A.: Visualization, Validation, Methodology, Data Curation, Investigation, Writing – Review & Editing. M.S.I.M.: Methodology, Visualization, Investigation, Writing - Review & Editing. S.C.P.: Formal analysis, Visualization, Suggestion, Writing – Review & Editing; M.J.H.M.: Formal analysis, Visualization, Data Curation, Investigation. M.M.A.S.: Review, Suggestion, Administration and Supervision. All authors have read and agreed to the published version of the manuscript.

Acknowledgements

All authors want to show thankfulness to each contribution for accomplishing this research work.

References

- [1] Saury, D., Rouger, N., Djanna, F. and Penot, F. Natural convection in an air-filled cavity: experimental results at large Rayleigh numbers. *International Communications in Heat and Mass Transfer*, 38(6), 679-687, (2011). [[CrossRef](#)]
- [2] Sajjadi, H., Gorji, M., Kefayati, G.H.R., Ganji, D.D. and Shayan Nia, M. Numerical analysis of turbulent natural convection in a square cavity using Large-Eddy simulation in lattice Boltzmann method. *Iranian Journal of Science & Technology Transactions of Mechanical Engineering*, 35(M2), 33-143, (2011). [[CrossRef](#)]
- [3] Shati, A.K.A., Blakey, S.G. and Beck, S.B.M. A dimensionless solution to radiation and turbulent natural convection in square and rectangular enclosures. *Journal of Engineering Science and Technology*, 7(2), 257-279, (2012).
- [4] Durand-Estebe, B., Lebot, C., Arquis, E. and Mancos, J. Validation of turbulent natural convection in a square cavity for application of CFD modeling to heat transfer and fluid flow in a data center. In *Proceedings, Biennial Conference on Engineering Systems Design and Analysis (ESDA)*, pp. 111-127, Nantes, France, (2012, July).
- [5] Choi, S.K. and Kim, S.O. Turbulence modeling of natural convection in enclosures: a review. *Journal of Mechanical Science and Technology*, 26, 283-297, (2012). [[CrossRef](#)]
- [6] Jani, S., Mahmoodi, M. and Amini, M. Magnetohydrodynamic free convection in a square cavity heated from below and cooled from other walls. *International Journal of Mechanical, Industrial Science and Engineering*, 7(4), 750-755, (2013).
- [7] Butler, C., Newport, D. and Geron, M. Natural convection experiments on a heated horizontal cylinder in a differentially heated square cavity. *Experimental Thermal and Fluid Science*, 44, 199-208, (2013). [[CrossRef](#)]
- [8] Xin, S., Salat, J., Joubert, P., Sergent, A., Penot, F. and Le Quéré, P. Resolving the stratification discrepancy of turbulent natural convection in differentially heated air-filled cavities. Part III: A full convection–conduction–surface radiation coupling. *International Journal of Heat and Fluid Flow*, 42, 33-48, (2013). [[CrossRef](#)]
- [9] Carvalho, P.H.S. and De Lemos, M.J.S. Turbulent free convection in a porous square cavity using the thermal equilibrium model. *International Communications in Heat and Mass Transfer*, 49, 10-16, (2013). [[CrossRef](#)]
- [10] Kefayati, G.H. Lattice Boltzmann simulation of natural convection in a nanofluid-filled inclined square cavity at presence of magnetic field. *Scientia Iranica*, 20(5), 1517-1527, (2013). [[CrossRef](#)]
- [11] Bahoosh, R., Mohamadi, F. and Karimi, M. Numerical investigation of natural convection in a square cavity with tilting walls. *Journal of Thermophysics and Heat Transfer*, 29(4), 725-731, (2014). [[CrossRef](#)]
- [12] Jani, S., Mahmoodi, M., Amini, M. and Jam, J.E. Numerical investigation of natural convection heat transfer in a symmetrically cooled square cavity with a thin fin on its bottom wall. *Thermal Science*, 18(4), 1119-1132, (2014). [[CrossRef](#)]
- [13] Asad, M.F.A., M., Oreyeni, T., Yavuz, M. and Olanrewaju, P.O. Analytic simulation of MHD boundary layer flow of a chemically reacting upper-convected Maxwell fluid past a vertical

- surface subjected to double stratifications with variable properties. *The European Physical Journal Plus*, 137, 813, (2022). [[CrossRef](#)]
- [14] Islam, T., Yavuz, M., Parveen, N. and Asad, M.F.A. Impact of non-uniform periodic magnetic field on unsteady natural convection flow of nanofluids in square enclosure. *Fractal and Fractional*, 6(2), 101, (2022). [[CrossRef](#)]
- [15] Asad, M.F.A., Yavuz, M., Alam, M.N., Sarker, M.M.A. and Bazighifan, O. Influence of fin length on magneto-combined convection heat transfer performance in a lid-driven wavy cavity. *Fractal and Fractional*, 5(3), 107, (2021). [[CrossRef](#)]
- [16] Sajjadi, H. and Kefayati, R. Lattice Boltzmann simulation of turbulent natural convection in tall enclosures. *Thermal Science*, 19(1), 155-166, (2015). [[CrossRef](#)]
- [17] Miroshnichenko, I. and Sheremet, M. Comparative study of standard $k - \epsilon$ and $k - \epsilon$ turbulence models by giving an analysis of turbulent natural convection in an enclosure. In *EPJ Web of Conferences*, 82, 1-4, (2015). [[CrossRef](#)]
- [18] Zineddine, D.A., Tabet, S. and Azzi, A. Natural convection in partially heated square cavity. *Mechanics*, 22(2), 119-124, (2016). [[CrossRef](#)]
- [19] Zhao, B. and Tian, Z. High-resolution high-order upwind compact scheme-based numerical computation of natural convection flows in a square cavity. *International Journal of Heat and Mass Transfer*, 98, 313-328, (2016). [[CrossRef](#)]
- [20] Aithal, S.M. Turbulent natural convection in a square cavity with a circular cylinder. *Journal of Thermo physics and Heat Transfer*, 30(4), 843-853, (2016). [[CrossRef](#)]
- [21] Adnani, M., Meziani, B., Ourrad, O. and Zitoune, M. Natural convection in a square cavity: numerical study for different values of prandtl number. *Fluid Dynamics and Material Processing*, 12(1), 1-14, (2016).
- [22] Benchabi, R. and Lanani, A. Two-Dimensional numerical simulation of natural convection in a square cavity. *Mechanics*, 23(4), 545-551, (2017). [[CrossRef](#)]
- [23] Solomon, A.B., van Rooyen, J., Rencken, M., Sharifpur, M. and Meyer, J.P. Experimental study on the influence of the aspect ratio of square cavity on natural convection heat transfer with Al₂O₃/Water nanofluids. *International Communications in Heat and Mass Transfer*, 88, 254-261, (2017). [[CrossRef](#)]
- [24] Yang, G., Iacovides, H., Craft, T. and Apsley, D. RANS modelling for temperature variance in conjugate heat transfer. In *Proceedings 5th World Congress on Mechanical, Chemical, and Material Engineering*, pp. 15-17, Lisbon, Portugal, (2019, August). [[CrossRef](#)]
- [25] Razera, A.L., da Fonseca, R.J.C., Isoldi, L.A., Dos Santos, E.D., Rocha, L.A.O. and Biserni, C. A constructal approach applied to the cooling of semi-elliptical blocks assembled into a rectangular channel under forced convection. *International Journal of Heat and Mass Transfer*, 184, 122293, (2022). [[CrossRef](#)]
- [26] Selimefendigil, F. and Öztop, H.F. Optimization of convective heat transfer performance for fluid flow over a facing step by using an elliptic porous object. *Case Studies in Thermal Engineering*, 27, 101233, (2021). [[CrossRef](#)]
- [27] Khatamifar, M., Lin, W. and Dong, L. Transient conjugate natural convection heat transfer in a differentially-heated square cavity with a partition of finite thickness and thermal conductivity. *Case Studies in Thermal Engineering*, 25, 100952, (2021). [[CrossRef](#)]
- [28] Devi, T.S., Lakshmi, C.V., Venkatadri, K. and Reddy, M.S. Influence of external magnetic wire on natural convection of non-Newtonian fluid in a square cavity. *Partial Differential Equations*

in *Applied Mathematics*, 4, 100041, (2021). [[CrossRef](#)]

- [29] Wen, X., Wang, L.P. and Guo, Z. Development of unsteady natural convection in a square cavity under large temperature difference. *Physics of Fluids*, 33, 084108, (2021). [[CrossRef](#)]
- [30] Goswami, N., Randive, P.R. and Pati, S. Natural convection from a pair of heated cylinders in a square cavity with non-uniform temperature on the side walls. *Journal of The Institution of Engineers (India): Series C*, 102, 389-396, (2021). [[CrossRef](#)]
- [31] El, H.M. and Lafdaili, Z. Turbulent natural-convection heat transfer in a square cavity with nanofluids in presence of inclined magnetic field. *Thermal Science*, 26(4), 3201-3213, (2022).
- [32] Turkyilmazoglu, M. Exponential nonuniform wall heating of a square cavity and natural convection. *Chinese Journal of Physics*, 77, 2122-2135, (2022). [[CrossRef](#)]
- [33] Bilal, S., Khan, N.Z., Shah, I.A., Awrejcewicz, J., Akgül, A. and Riaz, M.B. Numerical study of natural convection of power law fluid in a square cavity fitted with a uniformly heated T-fin. *Mathematics*, 10(3), 342, (2022). [[CrossRef](#)]
- [34] Sondur, S.R., Meuris, B. and Mescher, A.M. Benchmarked simulations of natural convection airflow in a square cavity. *Numerical Heat Transfer, Part A: Applications*, 84(4), 297-314, (2023). [[CrossRef](#)]
- [35] Asad, M.F.A., Alam, M.N., Tunç, C. and Sarker, M.M.A. Heat transport exploration of free convection flow inside enclosure having vertical wavy walls. *Journal of Applied and Computational Mechanics*, 7(2), 520-527, (2021). [[CrossRef](#)]
- [36] Asad, M.F.A., Alam, M.N., Rashad, A.M. and Sarker, M.M.A. Impact of undulation on magneto-free convective heat transport in an enclosure having vertical wavy sides. *International Communications in Heat and Mass Transfer*, 127, 105579, (2021). [[CrossRef](#)]
- [37] Hossain, M.S., Asad, M.F.A., Mallik, M.S.I., Yavuz, M., Alim, M.A. and Khairul Basher, K.M. Numerical study of the effect of a heated cylinder on natural convection in a square cavity in the presence of a magnetic field. *Mathematical and Computational Applications*, 27(4), 58, 1-17, (2022). [[CrossRef](#)]
- [38] Asad, M.F.A., Alam, M.N., Ahmad, H., Sarker, M.M.A., Alsulami, M.D. and Gepreel, K.A. Impact of a closed space rectangular heat source on natural convective flow through triangular cavity. *Results in Physics*, 23, 104011, (2021). [[CrossRef](#)]
- [39] Hossain, M.S., Sarder, C.K., Hoque, K.E., Bangalee, M.Z.I., Billah, M.M. and Uddin, M.A. Finite element simulation on MHD free convection in a square enclosure with elliptical shaped obstacle. *Ganit: Journal of Bangladesh Mathematical Society*, 43(1), 63-75, (2023).
- [40] Hossain, M.S., Alim, M.A. and Andallah, L.S. Numerical simulation of MHD natural convection flow within porous trapezoidal cavity with heated triangular obstacle. *International Journal of Applied and Computational Mathematics*, 6, 166, (2020). [[CrossRef](#)]
- [41] Hossain, M.S. and Alim, M.A. MHD free convection within trapezoidal cavity with non-uniformly heated bottom wall. *International Journal of Heat and Mass Transfer*, 69, 327–336, (2014). [[CrossRef](#)]
- [42] Hossain, M.S., Alim, M.A. and Andallah, L.S. Numerical investigation of natural convection flow in a trapezoidal cavity with non-uniformly heated triangular block embedded inside. *Journal of Advances in Mathematics and Computer Science*, 28(5), 1-30, (2018). [[CrossRef](#)]
- [43] Taylor, C. and Hood, P. A numerical solution of the Navier-Stokes equations using the finite element technique. *Computers & Fluids*, 1(1), 73-100, (1973). [[CrossRef](#)]

- [44] Reddy J.N. An introduction to the finite element method. In *Dynamics of Earth's Fluid System* (pp.). McGraw-Hill, New York, 1985.
- [45] Rahman, M.M., Alim, M.A. and Mamun, M.A.H. Finite element analysis of mixed convection in a rectangular cavity with a heat-conducting horizontal circular cylinder. *Nonlinear Analysis: Modelling and Control*, 14(2), 217-247, (2009).

Mathematical Modelling and Numerical Simulation with Applications (MMNSA)
(<https://dergipark.org.tr/en/pub/mmnsa>)



Copyright: © 2024 by the authors. This work is licensed under a Creative Commons Attribution 4.0 (CC BY) International License. The authors retain ownership of the copyright for their article, but they allow anyone to download, reuse, reprint, modify, distribute, and/or copy articles in MMNSA, so long as the original authors and source are credited. To see the complete license contents, please visit (<http://creativecommons.org/licenses/by/4.0/>).

How to cite this article: Billah, S.S., Hossain, M.S., Asad, M.F.A., Mallik, M.S.I., Paul, S.C., Munshi, M.J.H. & Sarker, M.M.A. (2024). Free convection at different locations of adiabatic elliptic blockage in a square enclosure. *Mathematical Modelling and Numerical Simulation with Applications*, 4(1), 86-109. <https://doi.org/10.53391/mmnsa.1382516>